Earth and Planetary Science Letters 454 (2016) 178–191

Contents lists available at ScienceDirect

Earth and Planetary Science Letters

www.elsevier.com/locate/epsl

Effects of water transportation on subduction dynamics: Roles of viscosity and density reduction

Atsushi Nakao [a,b,*], Hikaru Iwamori [a,b], Tomoeki Nakakuki [c]

[a] Department of Earth and Planetary Sciences, Tokyo Institute of Technology, 2-12-1 Ookayama, Meguro-ku, Tokyo, 152-8550, Japan
[b] Department of Solid Earth Geochemistry, Japan Agency for Marine–Earth Science and Technology, 2-15 Natsushima-cho, Yokosuka, Kanagawa 237-0061, Japan
[c] Department of Earth and Planetary Systems Science, Hiroshima University, 1-3-1 Kagamiyama, Higashi-Hiroshima, Hiroshima 739-8526, Japan

ARTICLE INFO

Article history:
Received 4 March 2016
Received in revised form 12 July 2016
Accepted 9 August 2016
Available online 21 September 2016
Editor: B. Buffett

Keywords:
water transportation
free convection
subduction dynamics
plate velocity
stagnant slab
trench migration

ABSTRACT

The effects of water on subduction dynamics, e.g., plate migration rate, slab geometry, stress field, and back-arc spreading, are investigated by using a 2-D self-consistent model for lithosphere subduction and whole mantle convection. We solve water transportation coupled with hydrous mineral phase changes. Mantle flows and water transportation are interactive through constitutive and state equations for hydrous rocks. Our model has successfully reproduced the water distribution in a mantle wedge and along the slab with sufficient resolution comparable to that of previous models that focus on the mantle wedge structure. As a result, low density owing to hydration reduces subduction rates, back-arc spreading, and slab stagnation on the phase boundary at 660-km depth, whereas low viscosity owing to hydration enhances rapid subduction, trench migration, and slab stagnation. We attribute these results to mechanisms that cause the hydrous buoyancy of subducting plates to reduce the slab pull force and the accompanying tensile stress on overlying lithosphere. In addition, hydrous weakening diminishes the mechanical coupling of the subducted slab with the wedge mantle and overriding lithosphere. Thus, water is capable of generating two opposite situations in the stress field of the overlying lithosphere and the subduction rate. Water is therefore expected to be an important mechanism for generating broad styles of the subduction structure and kinematics, as observed in actual subduction zones such as Tonga and Mariana. Such observed variation in the subduction mode can be caused by variation in buoyancy corresponding to the water content from relatively dry to several thousands of parts per million for the wedge mantle and slab surface, whereas the extremely buoyant case does not appear to occur in nature. Water in the mantle is thus key to better understand the whole-mantle-scale slab dynamics as well as island arc volcanic processes.

1. Introduction

It is widely accepted that the Earth's mantle contains water in several tens to several hundreds of parts per million according to electrical conductivity measurements of hydrous minerals and electromagnetic observations (Karato, 2011). Water in rocks causes subduction initiation (Van der Lee et al., 2008), low viscosity of the asthenosphere (Karato and Jung, 1998), magmatism in volcanic arcs (Iwamori, 1998), fault zones (Wannamaker et al., 2009), and deeper earthquakes (Yamasaki and Seno, 2003). Experimental studies have quantified the viscosity and the density of hydrous rocks, both of which are much smaller than those of dry rocks (e.g., Hirth and Kohlstedt, 2003; Inoue et al., 1998). The introduction of constitutive and state equations of hydrous rocks to fluid mechanical simulations enables assessment of the effects of water on mantle dynamics such as thinning of the overlying lithosphere (Arcay et al., 2005), growth of an accretion wedge and back-arc spreading owing to weak hydrous rocks and melts (Gerya and Meilick, 2011), and rapid water transportation by "wet plumes" of buoyant hydrous rocks above stagnant slabs (Richard and Iwamori, 2010).

These previous numerical studies have provided invaluable insight into the role of water in subduction zones by highlighting the individual physical and chemical influences of water on the wedge mantle and the overriding plate. Because of the limitation of the model domains, the influences of water on subduction dynamics including plate motions have been scarcely debated. Numerical and laboratory simulations of free convection show re-

* Corresponding author at: Department of Earth and Planetary Sciences, Tokyo Institute of Technology, 2-12-1 Ookayama, Meguro-ku, Tokyo, 152-8550, Japan.
E-mail addresses: a.nakao@geo.titech.ac.jp, atsushi.nakao@gmail.com (A. Nakao).

http://dx.doi.org/10.1016/j.epsl.2016.08.016

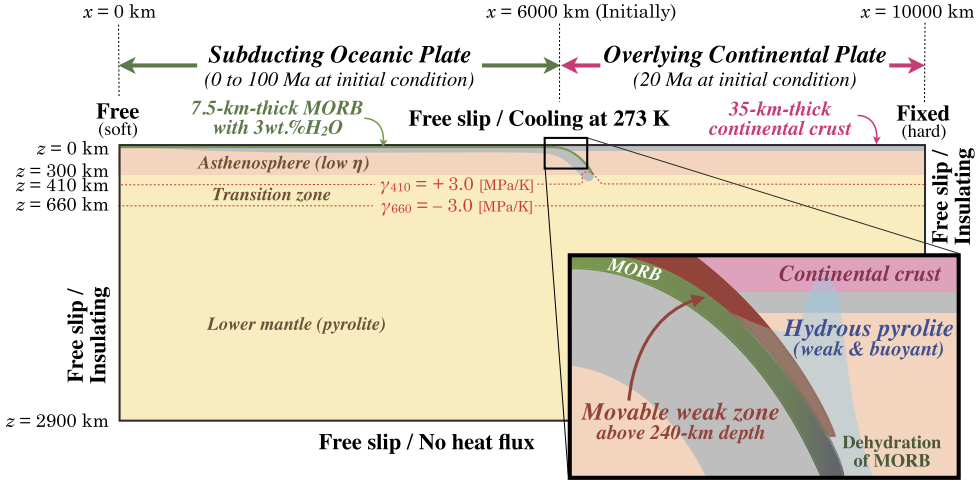

Fig. 1. Schematic diagram of the 2-D convection model. Details are described in Section 2.1.

markable acceleration/deceleration of subducting slabs associated with phase transition (e.g., Nakakuki and Mura, 2013; Schellart, 2008). In addition, seafloor age distribution analysis has revealed that the generation rates of oceanic plates have varied during the past 100 Myr (Conrad and Lithgow-Bertelloni, 2007), indicating inconstant subduction velocities in nature. However, it is still challenging to combine water transportation with a whole-mantle scale model because fine resolution is required to simulate water transportation and to apply actual rheology near the subduction zone.

This study seeks to determine the effects of water transportation on the behavior of the sinking and overlying plates integrated into the whole mantle convection. We focus on the velocity of the plates, slab deformation, the stress field of the overlying plate, and back-arc spreading by constructing a numerical model with the following characteristics: (1) free convection of whole-mantle scale without imposing velocity boundary conditions (e.g., Tagawa et al., 2007; Nakakuki and Mura, 2013), (2) phase diagrams of hydrous peridotite and hydrous basalt (Iwamori, 2007) to introduce hydration and dehydration reactions, and (3) properties of hydrous rocks formularized in constitutive and state equations. Introducing (3) makes (1) and (2) interactive. Regarding (3), we apply Arrhenius-type rheology functions for wet crystals determined experimentally (e.g., Hirth and Kohlstedt, 2003; Korenaga and Karato, 2008) and density reduction proportional to its water content (e.g., Richard and Iwamori, 2010; Horiuchi and Iwamori, 2016), both of which have been often simplified or not considered in previous studies (e.g., Rüpke et al., 2004; Arcay et al., 2005; Gerya and Meilick, 2011). Through these effects of hydration on rock properties, our simulation will demonstrate that water is not just a passive tracer in mantle flows but is an important factor in the changes of mantle flows and slab behavior.

2. Numerical settings and basic equations

2.1. Design of 2-D model and initial conditions

The 2-D domain of our model (Fig. 1) is 10,000 km in width × 2,900 km in length and includes phase boundaries at 410-km and 660-km depths, of which the effects on temperature and density are quantified in the energy conservation equation (Section 2.3) and the state equation (Section 2.5). Free slip conditions are imposed along top, bottom, and side boundaries so that the plate migration rates are controlled by the balance between the buoyancy and viscous resistance. This enables us to evaluate the effects of water on these rates. Surface temperature is constant at 273 K; therefore, as an oceanic plate migrates toward the right, the plate becomes thick as a result of cooling. Otherwise, no heat flux from the core to the mantle is assumed. In addition, insulating conditions are imposed along the side boundaries. The initial temperature of the lithosphere is determined from a cooling half-space model. The initial age of the oceanic plate is 0 Ma at the mid-ocean ridge and 100 Ma at the trench, and the initial age of the continental plate is 20 Ma. A thin, movable, and deformable weak zone dipping 27° mimicking a plate boundary is initially placed at a location 6,000 km from the left boundary. This segment has low yield strength (Section 2.4) and is transported by mantle flows (Section 2.6). Accordingly, the thickness and the angle of the weak zone change with the passage of time without synthetic forces. Although the segment extends along the slab, it does not reflect the mantle rheology below 240-km depth. Moreover, a 7.5-km-thick slab of mid-ocean ridge basalt (MORB) and a 35-km-thick slab of continental crust are placed along the surface, both of which are transported by convection.

The model domain is much larger than that of previous 2-D models (Arcay et al., 2005; Gerya and Meilick, 2011; Horiuchi and Iwamori, 2016). In order to derive fine solution around the subduction zones without consuming extensive computation time, we used a dual grid system developed by Tagawa et al. (2007), which includes a variable grid for equation of motion (Section 2.2) and a uniform grid for heat and marker transportation (Sections 2.3 and 2.6).

2.2. Mass and momentum conservation

All symbols used in the following equations are listed in Table 1.

We assume the mantle to be a 2-D incompressible, highly viscous fluid, the motion of which can be described as

$$\left(\frac{\partial^2}{\partial x^2}-\frac{\partial^2}{\partial z^2}\right)\left[\eta\left(\frac{\partial^2\psi}{\partial x^2}-\frac{\partial^2\psi}{\partial z^2}\right)\right]+4\frac{\partial^2}{\partial x\partial z}\left(\eta\frac{\partial^2\psi}{\partial x\partial z}\right)=\frac{\partial\rho}{\partial x}g, \tag{1}$$

where stream function ψ is defined by

$$\boldsymbol{v}=(u,w)\equiv\left(\frac{\partial\psi}{\partial z},-\frac{\partial\psi}{\partial x}\right). \tag{2}$$

Because we introduce water-dependent viscosity η and density ρ (Sections 2.4 and 2.5), the motion of mantle rocks is affected by hydration–dehydration reactions.

Table 1
Physical parameters and variables. The influences of the parameters with daggers (†) are demonstrated in the supplementary material.

Symbols	Explanations	Values	Units	References
A	Pre-exponential factor in constitutive laws		$\mathrm{Pa}^{-n}\,\mathrm{s}^{-1}$	
A_1	for dry diffusion creep ($z > 300$ km)	4.3733×10^{-12}	$\mathrm{Pa}^{-1}\,\mathrm{s}^{-1}$	Nakakuki and Mura (2013)
A_2	for wet diffusion creep ($z > 300$ km)	(depends on r)	$\mathrm{Pa}^{-1}\,\mathrm{s}^{-1}$	This study
A_3	for dry dislocation creep ($z < 300$ km)	4.6546×10^{-11}	$\mathrm{Pa}^{-1}\,\mathrm{s}^{-1}$	Nakakuki and Mura (2013)
A_4	for wet dislocation creep ($z < 300$ km)	(depends on r)	$\mathrm{Pa}^{-1}\,\mathrm{s}^{-1}$	This study
c_Y	Friction coefficient of intact material	0.3	–	Byerlee (1978)
c_{YF}	Friction coefficient of fractured material	0.004	–	
C_{H_2O}	Water content in solid (weight fraction)		$\mathrm{kg\,kg}^{-1}$	
C_{OH^-}	OH^- content in solid (molar ratio)		$\mathrm{ppm\,H\,Si}^{-1}$	
C_p	Specific heat at constant pressure	1.2×10^3	$\mathrm{J\,K}^{-1}\,\mathrm{kg}^{-1}$	
d_{410}	Half thickness of the 410-km boundary	20	km	
d_{660}	Half thickness of the 660-km boundary	2	km	
E^*	Activation energy		$\mathrm{kJ\,mol}^{-1}$	
E_1^*	for dry diffusion creep ($z > 300$ km)	240	$\mathrm{kJ\,mol}^{-1}$	e.g., Karato and Wu (1993)
E_2^*	for wet diffusion creep ($z > 300$ km)	240	$\mathrm{kJ\,mol}^{-1}$	e.g., Karato and Wu (1993)
E_3^*	for dry dislocation creep ($z < 300$ km)	430	$\mathrm{kJ\,mol}^{-1}$	e.g., Karato and Wu (1993)
E_4^*	for wet dislocation creep ($z < 300$ km)	430	$\mathrm{kJ\,mol}^{-1}$	e.g., Karato and Wu (1993)
g	Gravity acceleration	10	$\mathrm{m\,s}^{-2}$	
h	Thickness of mantle	2,900	km	e.g., Dziewonski and Anderson (1981)
H^{mantle}	Internal heating of mantle	5.44×10^{-12}	$\mathrm{W\,kg}^{-1}$	cf. Turcotte and Schubert (2001)
H^{MORB}	Internal heating of MORB	5.44×10^{-11}	$\mathrm{W\,kg}^{-1}$	cf. Turcotte and Schubert (2001)
H^{granite}	Internal heating of granite	5.44×10^{-10}	$\mathrm{W\,kg}^{-1}$	cf. Turcotte and Schubert (2001)
k	Thermal conductivity	4.68	$\mathrm{W\,m}^{-1}$	
n_3	Stress exponent for dry dislocation creep	3.0	–	Karato and Wu (1993)
n_4	Stress exponent for wet dislocation creep	3.0	–	Karato and Wu (1993)
p	Pressure		Pa	
r	Power of the viscosity water dependence		–	
r_{diff}	for wet diffusion creep ($z > 300$ km)	0–1.93	–	e.g., Hirth and Kohlstedt (2003)
r_{disl}	for wet dislocation creep ($z < 300$ km)	0–1.95	–	e.g., Hirth and Kohlstedt (2003)
R	Gas constant	8.3145	$\mathrm{J\,mol}^{-1}\,\mathrm{K}^{-1}$	
t	Time		s	
T	Absolute temperature of mantle		K	
T_0	Temperature at the surface ($z = 0$)	273	K	
T_{410}	Temperature at the 410-km boundary	1,691	K	Nakakuki and Mura (2013)
T_{660}	Temperature at the 660-km boundary	1,818	K	Nakakuki and Mura (2013)
$\boldsymbol{v} = (u, w)$	Velocity field of mantle		$\mathrm{m\,s}^{-1}$	
V^*	Activation volume		$\mathrm{cm}^3\,\mathrm{mol}^{-1}$	
V_1^*	for dry diffusion creep ($z > 300$ km)	(depends on z)	$\mathrm{cm}^3\,\mathrm{mol}^{-1}$	Nakakuki and Mura (2013)
V_2^*	for wet diffusion creep ($z > 300$ km)	(depends on z)	$\mathrm{cm}^3\,\mathrm{mol}^{-1}$	Nakakuki and Mura (2013)
V_3^*	for dry dislocation creep ($z < 300$ km)	15	$\mathrm{cm}^3\,\mathrm{mol}^{-1}$	Karato and Wu (1993)
V_4^*	for wet dislocation creep ($z < 300$ km)	15	$\mathrm{cm}^3\,\mathrm{mol}^{-1}$	Karato and Wu (1993)
V_0	at $z = 0$ km to calculate LM viscosity	5	$\mathrm{cm}^3\,\mathrm{mol}^{-1}$	Karato and Wu (1993)
V_L	at $z = 2000$ km to calculate LM viscosity	4	$\mathrm{cm}^3\,\mathrm{mol}^{-1}$	Nakakuki and Mura (2013)
x	Lateral coordinate	0–10000	km	
z	Vertical coordinate	0–2900	km	
z_{410}	Depth of the 410-km boundary ($T = T_{410}$)	410	km	
z_{660}	Depth of the 660-km boundary ($T = T_{660}$)	660	km	
α	Thermal expansivity	2.5×10^{-5}	K^{-1}	
β	Density water dependence coefficient	0–2	–	e.g., Jacobsen et al. (2008)
Γ_{410}	Function for smooth 410-km boundary		–	Christensen and Yuen (1985)
Γ_{660}	Function for smooth 660-km boundary		–	Christensen and Yuen (1985)
Γ_C	Function for smooth crust/mantle boundary		–	
γ_{410}	Clapeyron slope of the 410-km boundary	+3	$\mathrm{MPa\,K}^{-1}$	†
γ_{660}	Clapeyron slope of the 660-km boundary	−3	$\mathrm{MPa\,K}^{-1}$	†
$\Delta\rho_C$	Density contrast between granite and mantle	600	$\mathrm{kg\,m}^{-3}$	
$\Delta\rho_{410}$	Density contrast at the 410-km boundary	182.5	$\mathrm{kg\,m}^{-3}$	Dziewonski and Anderson (1981)
$\Delta\rho_{610}$	Density contrast at the 660-km boundary	194.2	$\mathrm{kg\,m}^{-3}$	Dziewonski and Anderson (1981)
$\dot{\varepsilon}, \dot{\varepsilon}_{ij}$	Strain rate		s^{-1}	
$\dot{\varepsilon}_{\mathrm{II}}$	Second invariant of strain rate		s^{-1}	
η	Effective viscosity of mantle	10^{17}–10^{25}	Pa s	
η_{ref}	Reference viscosity at 410-km depth	5×10^{20}	Pa s	e.g., Okuno and Nakada (2001)
σ, σ_{ij}	Stress		Pa	
σ_{II}	Second invariant of stress		Pa	
σ_Y	Yield strength		Pa	
σ_{Y0}	Cohesive strength	30	MPa	Byerlee (1978)
σ_{YF}	Cohesive strength at fractured areas		Pa	
$\sigma_{Y\max}$	Maximum yield strength	200	MPa	Kohlstedt et al. (1995) †
ψ	Stream function		$\mathrm{m}^2\,\mathrm{s}^{-1}$	
ρ	Density of mantle		$\mathrm{kg\,m}^{-3}$	
ρ_0	Reference density	3,900	$\mathrm{kg\,m}^{-3}$	
ρ_s	Density at the surface to calculate σ_Y	3,300	$\mathrm{kg\,m}^{-3}$	

Equation (1) is discretized by a finite volume method into a grid with 1346 × 306 nodes distributed non-uniformly. Areas with large viscosity or density gradients, e.g., near the plate boundary, hydrous zones, thermal boundary layers, and phase transition boundaries, are divided finely; the others, e.g., mid-lower mantle, are not. The minimum and maximum spacing are taken to be 2.5 km and 25 km, respectively.

One of the difficulties in solving a discretized equation of motion lies in deriving a robust solution under a large viscosity gradient. We applied the modified Cholesky decomposition algorithm, which is a direct solver of linear systems (e.g., Tagawa et al., 2007), although the direct method demands more computer resources than that of an iterative method.

2.3. Energy conservation

An equation of heat balance includes terms of thermal advection, adiabatic heating, latent heat due to the 410- and 660-km phase boundaries, thermal diffusion, viscous dissipation, and heat generation by radioactive elements,

$$\rho_0 C_p \left[\frac{\partial T}{\partial t} + \boldsymbol{v} \cdot \nabla T - w \frac{\alpha g T}{C_p} \right] + \gamma_{410} \frac{\Delta \rho_{410} T}{\rho_0} \frac{D\Gamma_{410}}{Dt} + \gamma_{660} \frac{\Delta \rho_{660} T}{\rho_0} \frac{D\Gamma_{660}}{Dt} = k \nabla^2 T + 4\eta \dot{\varepsilon}_{\mathrm{II}}^2 + \rho_0 H, \tag{3}$$

where Γ_{410}, Γ_{660}, and $\dot{\varepsilon}_{\mathrm{II}}$ are defined by

$$\Gamma_i = \frac{1}{2} \left[1 + \tanh \left(\frac{p - \rho_0 g z_i + \gamma_i (T - T_i)}{\rho_0 g d_i} \right) \right] \quad (i = 410, 660) \tag{4}$$

$$\dot{\varepsilon}_{\mathrm{II}} \equiv \sqrt{\frac{1}{2} \sum_{i,j=1}^{2} \dot{\varepsilon}_{ij}^2}. \tag{5}$$

Different internal heating H is imposed among the mantle (×1), oceanic crust (×10), and continental crust (×100) based on present-day estimation (Turcotte and Schubert, 2001). To derive the temperature field for successive time steps, Equation (3) is discretized into a uniform grid consisting of 4,000 × 1,160 square control volumes with a 2.5-km side using a partially upwind finite volume scheme (Clauser and Kiesner, 1987).

2.4. Rheology model

As suggested by experimental results, we assume that the deformation rate of the dry and wet rocks follows Arrhenius laws (e.g., Korenaga and Karato, 2008),

$$\dot{\varepsilon}_{1(\mathrm{diff,dry})} = A_1 \exp \left(-\frac{E_1^* + pV_1^*}{RT} \right) \sigma \tag{6}$$

$$\dot{\varepsilon}_{2(\mathrm{diff,wet})} = A_2 C_{\mathrm{OH^-}}^{r_{\mathrm{diff}}} \exp \left(-\frac{E_2^* + pV_2^*}{RT} \right) \sigma \tag{7}$$

$$\dot{\varepsilon}_{3(\mathrm{disl,dry})} = A_3 \exp \left(-\frac{2}{n_3 + 1} \frac{E_3^* + pV_3^*}{RT} \right) \sigma \tag{8}$$

$$\dot{\varepsilon}_{4(\mathrm{disl,wet})} = A_4 C_{\mathrm{OH^-}}^{r_{\mathrm{disl}}} \exp \left(-\frac{2}{n_4 + 1} \frac{E_4^* + pV_4^*}{RT} \right) \sigma . \tag{9}$$

Here, grain-size effects on diffusion creep are ignored. We approximate dislocation creep to linear creep with reduced activation enthalpy according to Christensen (1984). For simplification, the viscosity of MORB is assumed to be the same as that of the mantle.

We applied the values of activation energy E_i^* and activation volume V_i^* of the upper mantle estimated by Karato and Wu (1993) to the whole mantle; however, the viscosity of the lower mantle calculated from Arrhenius laws for olivine is much larger than that observed from postglacial rebound (e.g., Okuno and Nakada, 2001). In order to reduce the pressure dependence, the activation volume below 300-km depth is assumed to decrease linearly with the depth, i.e.,

$$V_{1,2}^* = V_0 + (V_L - V_0) \frac{z}{h}. \tag{10}$$

Because deformation in laboratories differs from that in Earth's mantle on both spatial and temporal scales, it is necessary to re-evaluate the viscosity scales A_i. A_1 is determined so that the viscosity calculated from the above constitutive law for dry diffusion creep corresponds to an estimation $\eta_{\mathrm{ref}} = 5 \times 10^{20}$ Pa s at the 410-km phase boundary (e.g., Okuno and Nakada, 2001). A_2 is determined so that the wet diffusion mechanism is dominant ($\dot{\varepsilon}_2 > \dot{\varepsilon}_1$) when the rock contains water above 100 ppm at the 410-km phase transition condition. The formulation is based on the assumption that the viscosity of the present-day mantle transition zone containing 100 ppm H_2O could be realized by both dry and wet diffusion mechanisms. A_3 and A_4, coefficients for dislocation creep, are determined so that dislocation creep becomes dominant ($\dot{\varepsilon}_3 > \dot{\varepsilon}_1$ and $\dot{\varepsilon}_4 > \dot{\varepsilon}_2$) above 300-km depth to reproduce the low viscosity of the asthenosphere.

The values of the water exponent r_{diff} and r_{disl} are treated as variable parameters owing to their uncertainty (Korenaga and Karato, 2008; Hirth and Kohlstedt, 2003; Fei et al., 2013). The meanings and origin of the uncertainty of r are discussed in Section 4.3.

Dry and wet deformation mechanisms simultaneously work on the same material. As $\dot{\varepsilon}_{\mathrm{dry}} \gg \dot{\varepsilon}_{\mathrm{wet}}$ in less-hydrated rocks and $\dot{\varepsilon}_{\mathrm{dry}} \ll \dot{\varepsilon}_{\mathrm{wet}}$ in well-hydrated rocks, the effective strain rate is approximated by the value of the dominant mechanism,

$$\dot{\varepsilon} = \max [\dot{\varepsilon}_1, \dot{\varepsilon}_2, \dot{\varepsilon}_3, \dot{\varepsilon}_4] . \tag{11}$$

In addition to creep mechanisms, in order to reproduce plate-like behavior, we introduce yielding of highly viscous fluid (e.g., Cserepes, 1982; Tackley, 2000). If stress reaches yield strength σ_{Y}, the viscosity significantly decreases, i.e.,

$$\eta = \frac{\sigma_{\mathrm{Y}}}{2\dot{\varepsilon}_{\mathrm{II}}} \quad (\sigma_{\mathrm{II}} = \sigma_{\mathrm{Y}}), \tag{12}$$

where $\dot{\varepsilon}_{\mathrm{II}}$ is defined by Equation (5). On the contrary, if the stress acting on the rock is smaller than the yield strength, the creep mechanisms dominate as defined by Equation (11),

$$\eta = \frac{\sigma_{\mathrm{II}}}{\dot{\varepsilon}_{\mathrm{II}}} \quad (\sigma_{\mathrm{II}} < \sigma_{\mathrm{Y}}). \tag{13}$$

The second invariant of stress is defined by

$$\sigma_{\mathrm{II}} \equiv \sqrt{\frac{1}{2} \sum_{i,j=1}^{2} \sigma_{ij}^2}. \tag{14}$$

The yield strength is assumed to increase linearly with the depth z, i.e.,

$$\sigma_{\mathrm{Y}} = \min[(\sigma_{\mathrm{Y0}} + c_{\mathrm{Y}} \rho_s g z), \sigma_{\mathrm{Ymax}}]. \tag{15}$$

The maximum yield strength σ_{Ymax} is determined as the brittle-ductile transition of the lithosphere (Kohlstedt et al., 1995). Although the larger σ_{Ymax} of the overlying lithosphere prevents trench motion and rapid subduction, we regard their effects on the subduction mode as minimal, as discussed in the supplementary

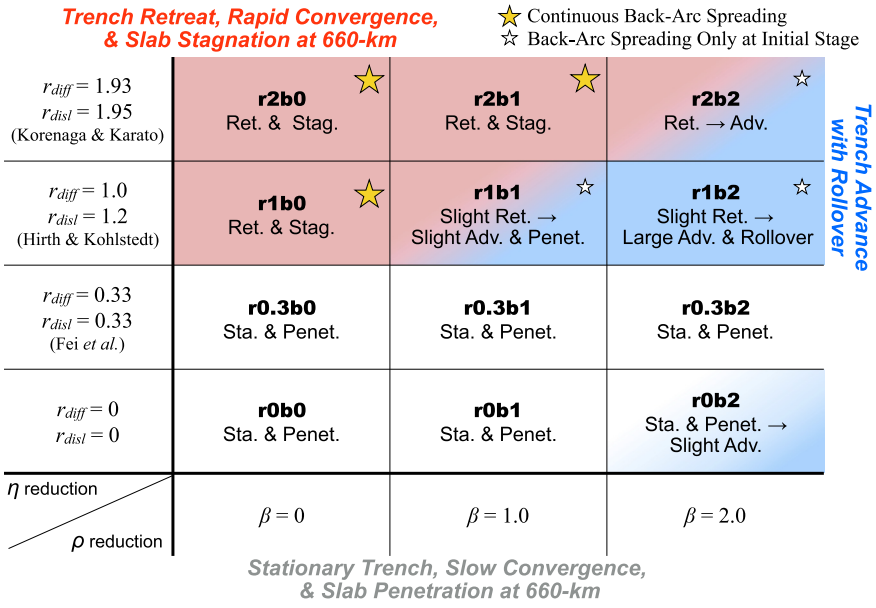

Fig. 2. Run list and the corresponding results diagram of all 12 cases with different hydrous weakening r (vertical) and hydrous buoyancy β (lateral).

materials. Small values of cohesive strength σ_{YF} and friction coefficient c_{YF} are imposed on the fault zone at $x = 6{,}000$ km and the mid-ocean ridge at $x = 0$ km. Contrary to that reported by Gerya and Meilick (2011), we do not incorporate the decline of lithospheric yield strength owing to hydration. Finally, the lower and upper limits of the effective viscosity are set to be 10^{17} and 10^{25} Pa s, respectively.

2.5. State equation

We calculate the buoyancy term in Equation (1) by introducing temperature-, water-, and phase-dependent density as

$$\rho = \rho_0 \left[1 - \alpha\,(T - T_0) - \beta C_{H_2O}\right] + \Delta\rho_{410}\Gamma_{410} + \Delta\rho_{660}\Gamma_{660} - \Delta\rho_C\Gamma_C. \quad (16)$$

After Jacobsen et al. (2008), Mao et al. (2008) and Inoue et al. (1998), β [(kg H_2O/kg)$^{-1}$] are 1.6 for olivine, 1.3 for wadsleyite, and 1.2 for ringwoodite. However, under a high-pressure condition, β is less constrained (Richard and Iwamori, 2010), and the value is treated as a variable. The meanings and origin of the uncertainty of β are discussed in Section 4.3.

The last three terms in Equation (16) are associated with the 410-km phase change, the 660-km phase change, and the continental crust, respectively. Density increases $\Delta\rho_{410}$ and $\Delta\rho_{660}$ are based on the Preliminary Reference Earth Model (PREM; Dziewonski and Anderson, 1981). Although Clapeyron slopes γ_{410} and γ_{660} are somewhat controversial, we verified that their effects on the subduction mode were minimal, as discussed in the supplementary materials. Γ_C is set to be 0 (peridotite) to 1 (continental crust). The density of MORB is assumed to be the same as that of mantle rocks.

2.6. Transportation of water and other materials

We assume that water bonded to or captured in minerals is transported with mantle flows, as expressed by the advection equation:

$$\frac{\partial C_{H_2O}}{\partial t} + \boldsymbol{v} \cdot \nabla C_{H_2O} = 0. \quad (17)$$

Here, hydrogen diffusion ($\kappa_H \ll 10^{-6}$ [m^2/s]; Mackwell and Kohlstedt, 1990; Sun et al., 2015) is ignored owing to the short calculation period (< 50 Myr). The advection term is calculated by a Marker-and-Cell method using 4,000 × 1,160 × 36 particles. We assume that MORB containing 3 wt.% H_2O sinks into an initially dry mantle (Rüpke et al., 2004; Horiuchi and Iwamori, 2016). The effects of water distribution in oceanic plates are verified in the supplementary materials: Given 6 wt.% H_2O within the uppermost oceanic crust, similar results were obtained. If C_{H_2O} in MORB or peridotite reaches the maximum water content determined by p–T phase diagrams of Iwamori (2007), excess aqueous fluid is emitted from the solid phase. Although the water storage capacity of the lower mantle is controversial, we assumed it to be 0.21 wt.% (Murakami et al., 2002) because we mainly simulated slab behavior in the upper mantle. In subduction zones with continuous dehydration, the upward velocity of the fluid flowing through porous media is 10^2 to 10^4 times higher than that of mantle flows (Iwamori, 1998). We therefore assume that all water released from the subducting slab is transported instantaneously upward and is absorbed into the overlying rocks that have available water capacity according to the p–T conditions, within one time step. In this way, water transportation can be simulated only by solving the equation of motion for the solid phase. The transportation of other heterogeneities such as MORB, continental crust, and fault segments also follows Equation (17) and is calculated by using the Marker-and-Cell method.

3. Results

In the following parameter study, two physical properties r (exponent of hydration-viscosity coefficient in the constitutive laws; Section 2.4) and β (hydration-density coefficient in the state equation; Section 2.5), are treated as variables; other settings and parameters are equalized. Twelve pairs of the parameters and the corresponding run IDs are listed in Fig. 2, and snapshots of all 12 runs are shown in Fig. 3.

3.1. Overview of water transportation

An example of the simulated evolution ($r_{diff} = 1.0$, $r_{disl} = 1.2$, $\beta = 1.0$) is shown in Fig. 4. The oceanic plate begins to

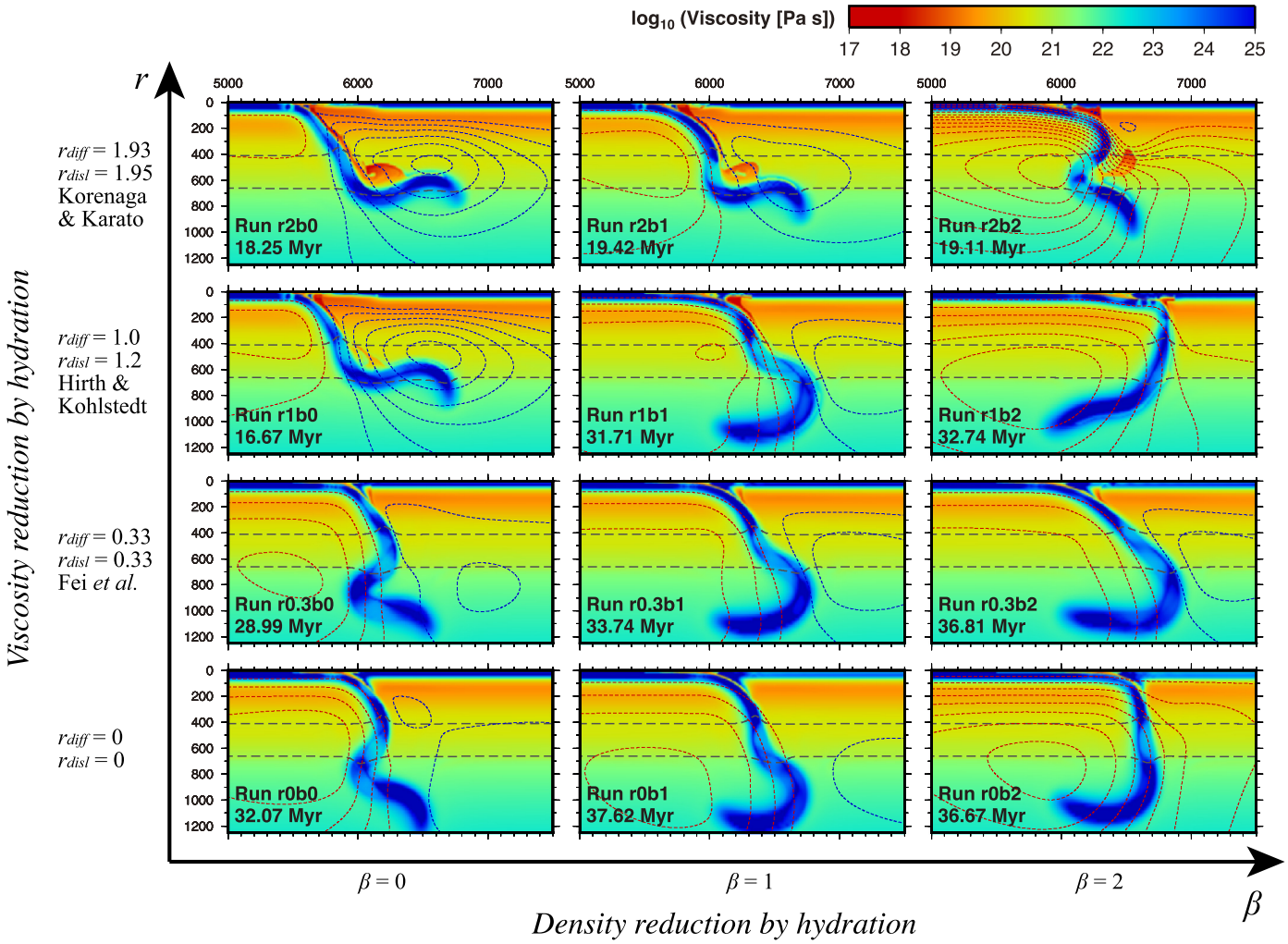

Fig. 3. Summary of all 12 runs with different hydrous weakening r (vertically) and hydrous buoyancy β (laterally). The colored contour shows viscosity structure. The presented range is horizontally $5{,}000 < x < 7{,}500$ [km] and vertically $0 < z < 1{,}250$ [km]. Red and blue dotted lines are clockwise ($\psi > 0$) and counterclockwise ($\psi < 0$) stream functions (10^{-4} [m^2/s] intervals), respectively. Dashed gray lines represent the 410-km and 660-km phase boundaries.

subduct as a result of its negative thermal buoyancy; correspondingly, the hydrous MORB layer sinks into the deep mantle (5.45 Myr in Fig. 4b, c). According to a phase diagram of hydrous basalt (Iwamori, 2007), MORB emits almost all water transforming into eclogite at a depth of about 70 km; accordingly, a layer of hydrous peridotite just above the subducted oceanic crust forms. Because the hydrous ultramafic layer still sinks, according to the phase diagram of hydrous peridotite of Iwamori (2007), dehydration reactions of hydrous minerals occur at about 600° ([8] Ol + Serp + Chl + Amp → [5] Ol + Opx + Chl + Cpx) and at about 800 °C ([5] → [1] Ol + Opx ± Pl/Sp/Gt ± Cpx) with the temperature increase owing to thermal conduction (7.65 Myr in Fig. 4b). This reaction path is the same as that of southwest Japan simulated by Iwamori (2007) using a wedge flow model. After that, the water fraction equal to the water storage capacity of nominally anhydrous minerals (NAMs) in assemblage [1], around 2,000 ppm, is transported by advection of the solid phase into the mantle transition zone without dehydration (8.61 Myr of Fig. 4b) because of the high water storage capacity of wadsleyite and ringwoodite (e.g., Inoue et al., 1995). These features were similarly reproduced by Horiuchi and Iwamori (2016), who considered the finite ascent velocity of aqueous fluid porous flow based on the same phase diagram and water storage capacity, which justifies the approximation of infinite ascent velocity in our model. In the case of $r_{\mathrm{diff}} \leq 1.0, r_{\mathrm{disl}} \leq 1.2$, despite hydrous weakening, the ultramafic hydrous layer is viscously coupled with the down-going slab without inducing wet plumes. This is in contrast to the results of Richard and Iwamori (2010), who considered the simple initial thermal structure of a slab. Excess water emitted from the ultramafic layer creates a low viscosity column from the slab surface to the shallow area (7.65 Myr in Fig. 4a), which is consistent with previous numerical studies (e.g., "thermal erosion of the overlapping lithosphere" of Arcay et al., 2005). Thus, lithosphere thinning occurs in the continental margin. Because the thermal effects on the viscosity are stronger than the hydrous effect, the cold upper continental lithosphere is sufficiently viscous. As a result, strong tensile stress working on the overlying lithosphere (5.45 Myr in Fig. 4c) induced by negative buoyancy of the subducting slab concentrates on the region of local erosion; correspondingly, the continental margin spreads by the yielding mechanism. While the yielding of the continental margin progresses, tensile stress working on the overlying lithosphere declines (5.45 Myr to 8.61 Myr in Fig. 4c). After that, with the hot asthenosphere welling to the surface, the overlying plate and continental crust separate (8.61 Myr in Fig. 4c). In this spreading mechanism, the stress concentration within the overlying lithosphere eroded by underlying hydration is the main cause for the back-arc opening. This differs from that proposed by Gerya and Meilick (2011), who argued for reduction of the yield strength of lithosphere owing to hydration. The gap

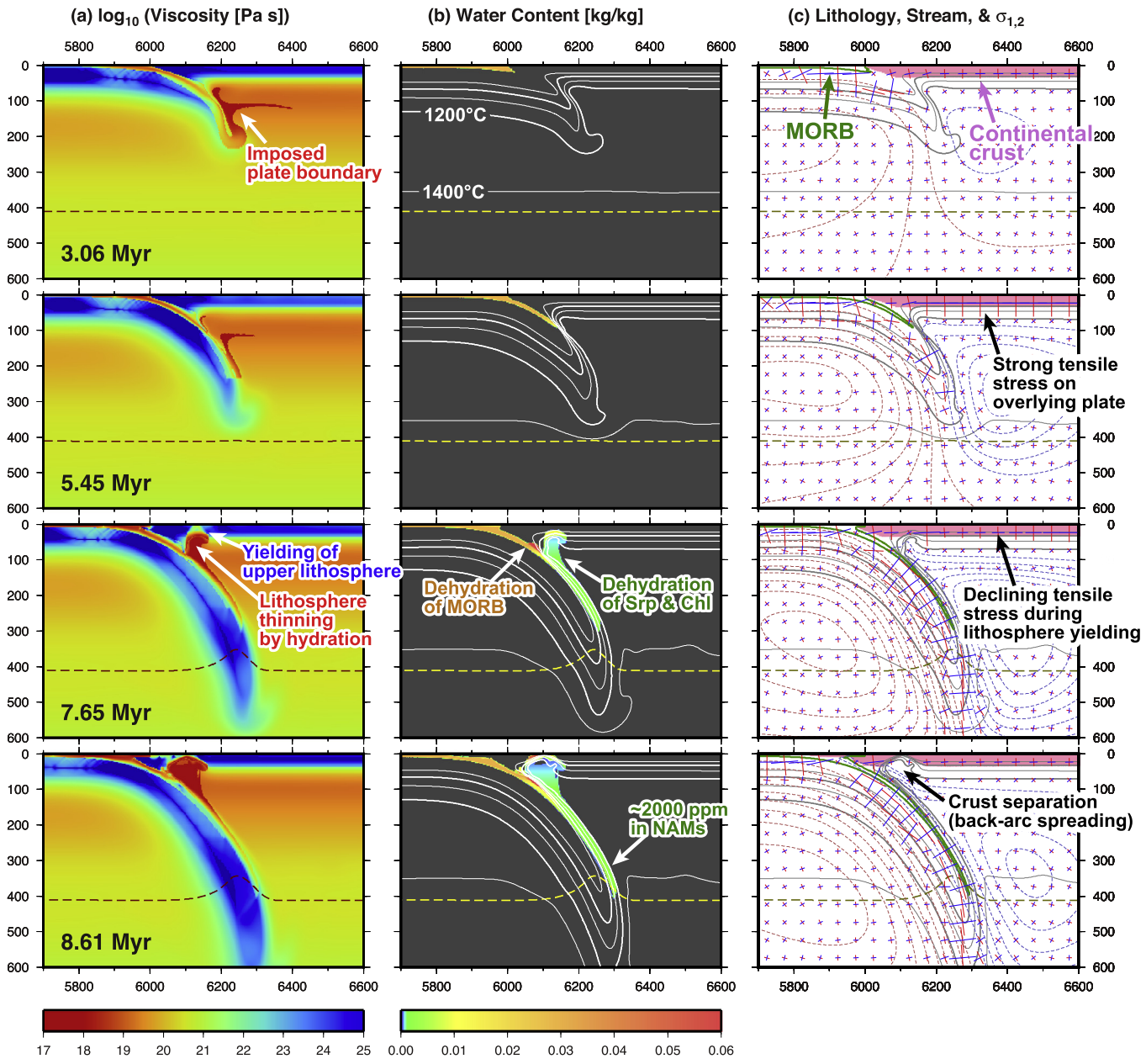

Fig. 4. Initial evolution of run r1b1 ($r_{diff} = 1.0, r_{disl} = 1.2, \beta = 1$). The presented range is horizontally $5{,}750 < x < 6{,}800$ [km] and vertically $0 < z < 600$ [km]. (a) The colored contour shows viscosity structure. Dashed brown lines represent the 410-km phase boundary. (b) The colored contour shows the weight fraction of water in rocks. White lines represent isotherms (200 °C intervals). Dashed yellow lines represent the 410-km phase boundary. (c) Pink and green areas show continental granite and oceanic basalt, respectively. Red and blue dotted lines are clockwise ($\psi > 0$) and counterclockwise ($\psi < 0$) stream functions (5×10^{-5} [m^2/s] intervals), respectively. Blue and red axes put at 50-km intervals represent the magnitude and directions of maximum principal stress σ_1 (tensile) and minimum principal stress σ_2 (compressive), respectively. Isotherms and the 410-km phase boundary are also shown.

enhances trench migration retreat or advance, depending on the parameter values, as will be discussed in the following sections.

3.2. *Effects of viscosity reduction owing to hydration*

Fig. 5 shows snapshots of four runs with different hydrous weakening r and the same hydrous buoyancy β. In the cases of larger r (Fig. 5a, b), erosion of the lower continental lithosphere hydrated through the porous flows from decomposed hydrous minerals plays an important role in causing the hot surrounding mantle to enter the shallower corner of the mantle wedge. As the slab reaches the 410-km phase boundary (i.e., the density of the slab increases due to the shallower phase change of olivine to wadsleyite), the continental margin is rapidly extended. This results in the intense trench retreat. Correspondingly, rapid flows are induced around the slab (i.e., closely plotted stream lines). Thereafter, a stagnant slab stably develops at the 660-km phase boundary. Although the scenarios of these two runs seem quite similar, evolution of run r2b0 is slightly faster than that of run r1b0 (Fig. 6). This is because the less viscous the hydrous layer and column are, the lower the viscous resistance around the slab is. Besides, given larger r, the ultramafic hydrous layer becomes less viscous, helping the hydrous rocks to separate from the slab surface.

In the cases of smaller r (Fig. 5c, d), although the hydrous layer and column also form, erosion of the lower continental lithosphere by hydration is slight or none. Such a thick continental margin prevents the concentration of tensile stress; therefore, neither back-arc spreading nor trench retreat occurs. The fixed trench causes slab penetration. The subduction rate in the case of lower r

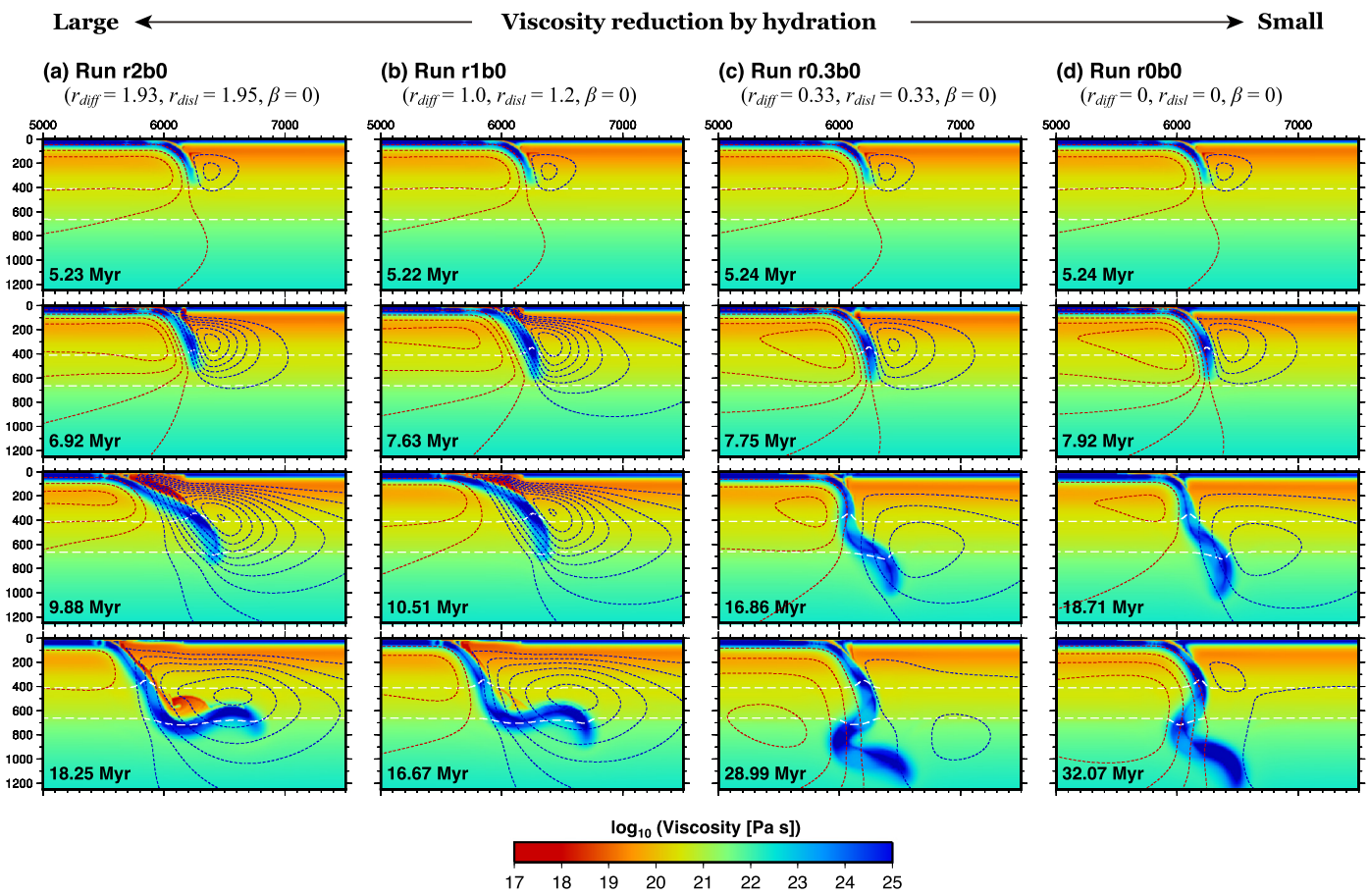

Fig. 5. Comparison of evolution of four runs, where different r (viscosity reduction by hydration) and the same β (= 0; hydrous buoyancy) are given. Symbols are the same as those in Fig. 3. (a) Evolution of run r2b0 ($r_{\mathrm{diff}} = 1.93, r_{\mathrm{disl}} = 1.95$). (b) Evolution of run r1b0 ($r_{\mathrm{diff}} = 1.0, r_{\mathrm{disl}} = 1.2$). (c) Evolution of r0.3b0 ($r_{\mathrm{diff}} = 0.33, r_{\mathrm{disl}} = 0.33$). (d) Evolution of r0b0 ($r_{\mathrm{diff}} = 0, r_{\mathrm{disl}} = 0$).

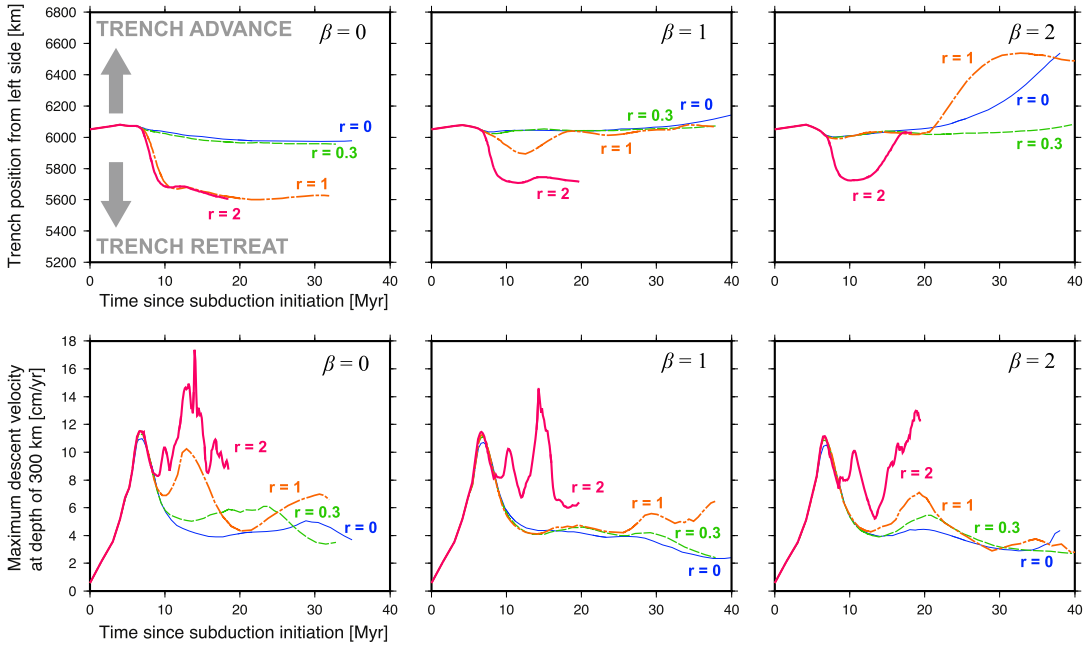

Fig. 6. Top three graphs denote time-dependent lateral positions of the trench of all 12 runs with different r (viscosity reduction by hydration) and β (density reduction by hydration), where the decline of the vertical value means trench retreat, and its increase means trench advance. The bottom three graphs similarly denote the maximum descent (vertical) velocity at a depth of 300 km.

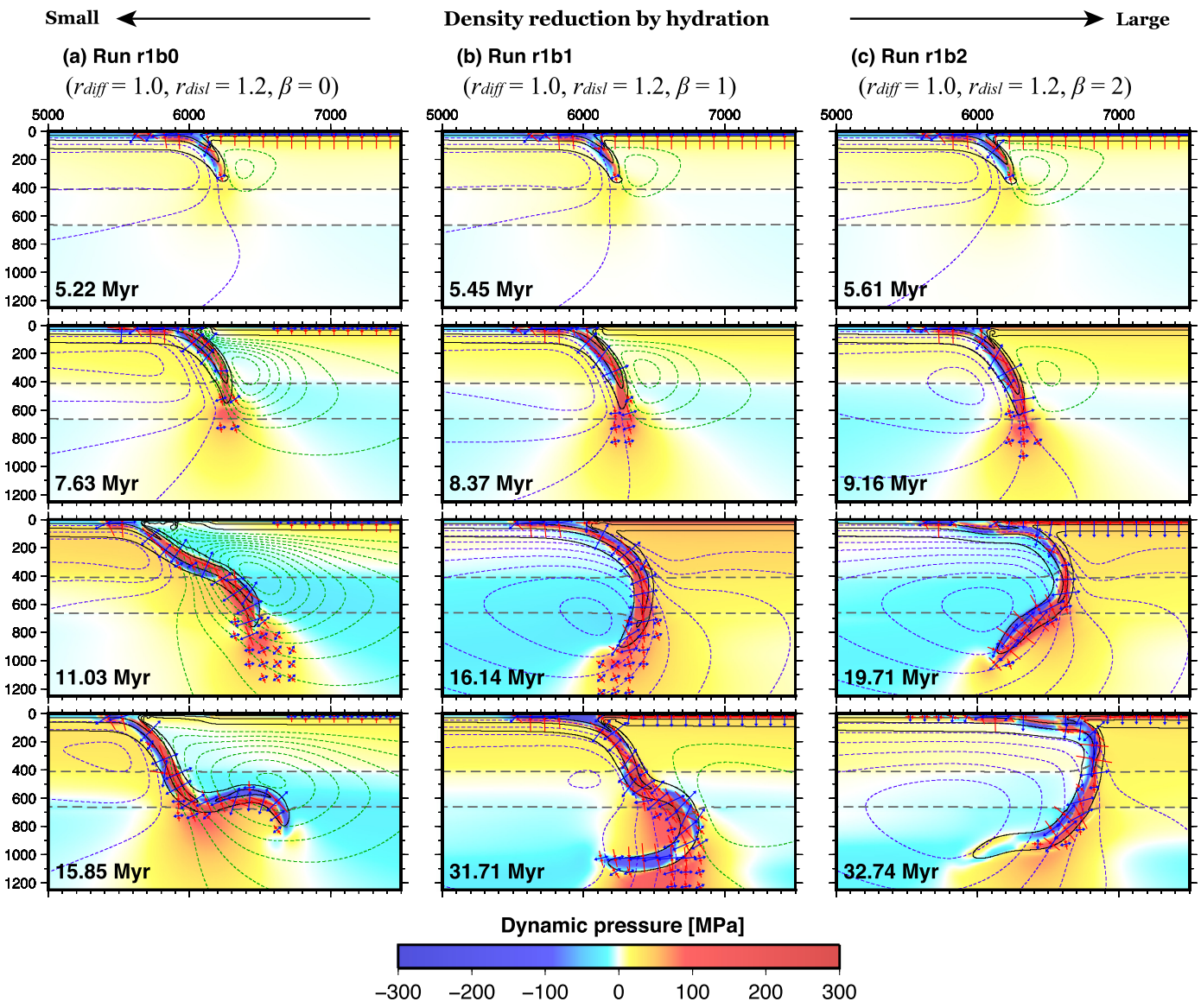

Fig. 7. Comparison between evolution of three runs, where varying β (hydrous buoyancy) and fixed r (= 1.0, 1.2; viscosity reduction by hydration) are given. The presented horizontal range is $5000 < x < 7500$ [km] and the vertical range is $0 < z < 1250$ [km]. The colored contour shows dynamic overpressure, or difference from lithostatic pressure; red areas are compressed, and blue areas are decompressed. Solid black lines represent isotherms (400 °C intervals). Purple and green dotted lines are clockwise ($\psi > 0$) and counterclockwise ($\psi < 0$) stream functions (10^{-4} [m^2/s] intervals), respectively. Blue and red arrows put at 150-km intervals represent magnitudes and directions of maximum principal stress σ_1 (tensile) and minimum principal stress σ_2 (compressive), respectively. Here we ignore arrows with small principal stress. Dashed gray lines represent 410- and 660-km phase boundaries. (a) Evolution of run r1b0 ($\beta = 0$). (b) Evolution of run r1b1 ($\beta = 1$). (c) Evolution of r1b2 ($\beta = 2$).

is much smaller (i.e., sparsely plotted stream lines) than that with larger r (Fig. 6). Similar to the runs with the stagnant slab formation, the evolution and subduction rates of run r0.3b0 are slightly higher than those of run r0b0, although these two results seem broadly similar.

Thus, viscosity reduction due to large r enhances trench migration and affects slab morphology. Note that transition between the retreating trench (and the corresponding stagnant slab) and the stationary trench (and the corresponding slab penetration) is related to yielding of the thinned continental margin; therefore, it is controlled not only by r but also by the thermal structure (i.e., thickness of the plate) and yield strength of the overlying plate. Moreover, since the especially small yield strength of hydrous lithosphere, which mimics fault activation by pore fluids, is not imposed, continental margins in nature may be extendable. In other words, after reaching the 660-km phase boundary, the slab does not penetrate further into the lower mantle, but tends to release its potential energy while the tip is anchored at the phase boundary owing to the higher viscosity of the lower mantle. This causes trench migration accompanied by extension of the deformable overriding plate due to a large r. Thus, we can consider that in runs with large r, slabs behave as if there is no overlying plate.

3.3. *Effects of density reduction owing to hydration*

Fig. 7 shows snapshots of three runs with varying hydrous buoyancy β and fixed hydrous weakening r. The dynamic pressure (difference from lithostatic pressure) displayed in Fig. 7 is solved using a SIMPLER algorithm (Patankar, 1981).

In the case of small β, Fig. 7a shows the same case as that of Fig. 5b, and we have already confirmed that tensile stress on the overlying plate, back-arc spreading, and trench retreat in run r1b0 are associated with a density increase in the slab due to Ol/Wd transition. During trench retreat and corresponding back-arc spreading, strong “downward” mantle flows (closely plotted stream functions) across the hydrous prism and layer in the edge of the

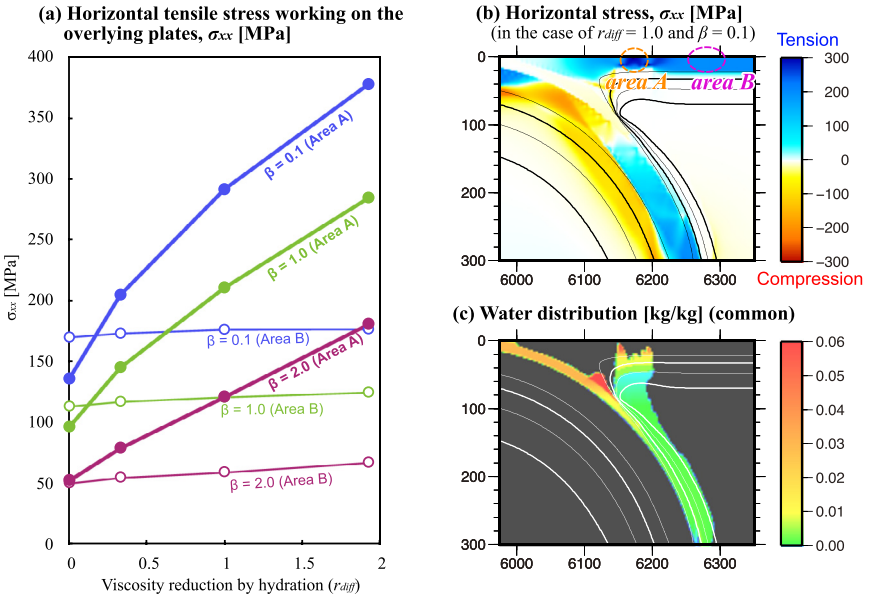

Fig. 8. (a) Horizontal tensile stress working on the overlying plates at 9.73 Myr (3,001st step). Results of all 12 runs are plotted here. Areas A (spreading region) and B (inland) are shown in (b). (b) Horizontal stress field at 9.73 Myr (3001st step) in run r1b0ny ($r_{\mathrm{diff}} = 1.0$, $r_{\mathrm{disl}} = 1.2$, $\beta = 0.1$). Positive values (cool color) mean laterally tensile and negative values (warm color) mean laterally compressive. Solid black lines represent 600, 800, 1,000, and 1,200 °C isotherms. (c) Water distribution at 9.73 Myr (3001st step) in the cases of all runs.

mantle wedge are induced to compensate for the retreating slab (7.63 to 11.03 Myr of Fig. 7a). Suction from the retreating slab induces negative dynamic pressure in the extending mantle wedge, and the overlying plate undergoes continuous tensile stress.

In the case of large β, as with run r1b0, back-arc spreading and trench retreat occur initially as the slab reaches the 410-km boundary. However, the retreat, induced corner flows, and subduction rate are less active than those in run r1b0 (Fig. 7b, c). The reason for this is that the buoyant hydrous areas along the slab surface partially cancel out the driving force of slab subduction, preventing the concentration of tensile stress enough to cause continental margin extension. As a result, the slab dip remains steep. After the slab crosses the 660-km boundary (i.e., the driving force diminishes), strong lateral flows directed from the oceanic asthenosphere to the continental side predominate (19.71 Myr of Fig. 7c) instead of the sub-continental "counterclockwise" streams that emerge in the trench retreat mode. This rightward flow compresses the hydrated mantle wedge and induces a correspondingly strong positive pressure. In contrast, the pressure at the rear of the advancing slab is negative, contributing to lifting of the tip of the slab in the lower mantle. The slab deformation causes maximum principal stress σ_1 (tensile axis) to turn along the slab in the lower mantle (19.71 Myr of Fig. 7c). The continuous-track-like shape accompanying trench advance occasionally emerges in previous laboratory and numerical experiments (e.g., Schellart, 2008; Stegman et al., 2010). This subduction structure would be the most efficient mode to release the potential energy of the cold slab so as to enable its descent into the deep mantle without dragging the buoyant hydrous rocks. In addition, the trench advance is also expected to be favorable to a small convergence rate owing to reduction of viscous dissipation by plate bending. These mechanisms to produce the trench motion are consistent with Royden and Husson (2006), who showed that the small buoyant "frontal prism" prevents the trench retreat and the formation of the gently-sloping slab.

Thus, hydrous buoyancy β contributes to slow subduction, slight back-arc spreading, compressive stress on the overlying plate associated with the 660-km-depth interaction, and the steep slab, all of which are roughly contrary to the effects of hydrous weakening r; however, the large (r, β) model, whose characteristics are the deforming continental margin and the movable trench (retreat to advance), is clearly different from the small (r, β) model, where both continental margin and trench are stationary.

3.4. Tensile stress acting on overlying plate

In the models described in the previous sections, yield strength is imposed on the lithosphere to provide the upper limit of the stress. This causes continental margin spreading, which induces the trench retreat and the slab stagnation. To quantify the potential for various r and β to generate tensile stress σ_{xx} in the overlying plate, we conducted a further simulation in which the yield strength was removed from the overriding lithosphere.

(Procedure 1) Before the 3,001st step (<9.73 Myr; after the tip of a slab enters the mantle transition zone; cf. the second panel of Fig. 5d), we conducted a common simulation employing the same method described in Chapter 2 using the same parameters as run r0b0.

(Procedure 2) At the 3,001st step (9.73 Myr), we removed yielding behavior (Equation (13)) from the overlying plate, and imposed 12 different (r, β) pairs on hydrous regions. Here we name them runs r0b0ny, r0b1ny, ... r2b2ny. We then solved the stream and the accompanying stress field at the time step. We calculate average σ_{xx} of the continental margin ("area A"; $6{,}170 < x < 6{,}180$ [km] and $2.5 < z < 10$ [km]) and the inland ("area B"; $6{,}250 < x < 6{,}300$ [km] and $2.5 < z < 10$ [km]).

The results are shown in Fig. 8. Values of σ_{xx} for area A increase with r, whereas σ_{xx} of area B is scarcely affected, suggesting that viscosity reduction by hydration, which competes with cooling of the plate, brings stress concentration. On the other hand, given reasonably larger hydrous buoyancy β, σ_{xx} on the overlying plate (both areas A and B) is diminished by several tens of percent. These features emerge significantly after the slab reaches the mantle transition zone.

In run r0.3b0ny, in which r and β are similar to runs without back-arc spreading (run r0.3b0; Fig. 5c), σ_{xx} on area A is much larger than yield strength ($50 < \sigma_{\mathrm{Y}} < 130$ [MPa]). This means that positive feedback between tensile stress concentration and lithosphere extension contribute significantly to back-arc spreading.

4. Discussion

4.1. Interpretation of subduction velocity change

We can easily understand how hydrous rock controls the subduction rate by quantifying the one-dimensional force balance around a slab

$$\int \{f_{\mathrm{T}}(l) \pm f_{\mathrm{P}}(l) - f_{\mathrm{H}}(\beta, l)\} \sin\theta dl + F_{\mathrm{top}} - \int \eta(r, l) \frac{du_{\mathrm{sp}}(h)}{dh} dl = 0 \quad (18)$$

where θ is the slab dip, and l and h are coordinates parallel/perpendicular to slab subduction. The first term is slab buoyancy controlled by heat (f_{T}), phase change (f_{P}), and hydration (f_{H}). The second term F_{top} represents the force acting on the top of the slab associated with ridge push. The third term is the viscous resistance acting along the slab. The subduction rate along the slab u_{sp} in the third term is controlled so as to be balanced with other forces. Given large hydrous weakening r, large u_{sp} is required to compensate for the reduction of $\eta(r)$ along a hydrous peridotite layer just above a slab (i.e., to keep the viscous resistance term). In contrast, given large hydrous buoyancy β, small u_{sp} is required to compensate for the reduction of the negative buoyancy. Thus, r and β play opposite roles in determining the subduction rate.

Initially (<7 Myr), the effects of f_{T} and f_{P} are dominant, whereas the effects of water are small. Thus, the acceleration of subduction in both cases is similar (Fig. 6). Deceleration after the first peak around 7 Myr corresponds to the contact between the slab tip and the 660-km phase boundary. Subsequently, a large subduction rate peak around 13 Myr in runs with large r corresponds to slab bending during trench retreat. In run r2b2, significant acceleration after 14 Myr would be caused by the collapse of a stagnant slab and/or thickened hydrous low-viscosity layer. After slab penetration, in runs with a semi-stationary trench (runs r1b1, r0.3b1, r0b1), the r effect emerges during semi-constant subduction (>15 Myr).

4.2. Insights into slab deformation and plate velocity

According to observations of plate motions and slab geometries, subduction styles in nature vary between two extreme modes (e.g., Schellart, 2011): one characterized by a rapid convergence rate, rapid trench retreat, and slab stagnation at the 660-km phase boundary, and the other by a slow convergence rate, a slightly advancing or stationary trench, and slab penetration into the lower mantle with steep dip. We can regard the Tonga and Mariana subduction zones as representatives of the end members. Fig. 9 shows the relationship between the convergence rate and trench migration of the global subduction zones (after Lallemand et al., 2008). Subduction zones with rapid convergence rates due to rapid trench retreat are observed where slabs make contact with the 660-km phase boundary (Tonga type). In contrast, the slab penetrating into the lower mantle has a noticeably slow convergence rate with advancing or stationary trench migration (Mariana type). The plate motions calculated in this study are consistent with the observational range, as shown in Fig. 9. The temporal variations of the convergence rate versus trench migration rate reproduce the observed variations depending on the (r, β) set (except for the slab rollover mode as will be described later), exhibiting a broad correlation between the trench migration and the convergence rate both in the natural and simulation systems.

The set of these features are reproduced in both numerical and laboratory experiments for “natural” or “forced” convection models (e.g., Schellart, 2011). This implies that the subduction mode is

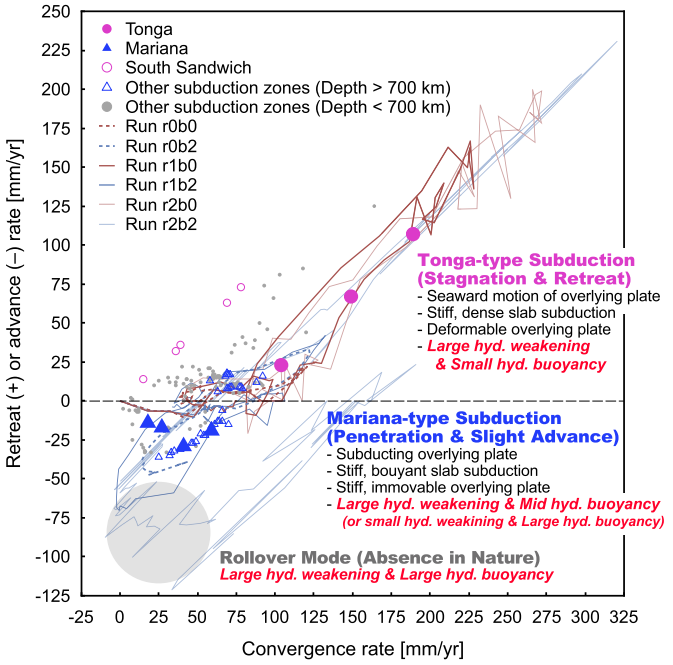

Fig. 9. Observed plate motions along subduction zones in the world. Data sets are referred from Lallemand et al. (2008) and are based on the plate model of Steinberger et al. (2004). The lateral axis indicates convergence rates between an oceanic plate and an overlying plate along a trench. The vertical axis indicates rates of trench motion; positive and negative values correspond to retreat and advance, respectively, and the horizontal dashed line represents the static trench. Large pink dots and large blue triangles represent the Tonga and Mariana regions, respectively. The South Sandwich subduction zone, where rapid trench retreat with slow subduction is exhibited by way of exception, is indicated by pinkish open circles. Data of other subduction zones are symbolized as small gray dots (slabs shallower than the 660-km phase boundary) and small blue opened triangles (slabs penetrating at the boundary). Possible tectonic forces and conditions that contribute to Tonga- and Mariana-type subduction are added to the figure. Convergence rates and trench movements of six runs (r2b0, r2b2, r1b0, r1b2, r0b0, and r0b2) are presented as tracks. The rollover mode with slow subduction and rapid trench advance, such as run r1b2 (Fig. 7c), is not observed in nature.

controlled by both “internal” and “external” forces. The tendency of dense slabs toward the Tonga-type mode and that of buoyant slabs toward the Mariana-type or rollover mode can be cited as instances of the influence of internal forces (Stegman et al., 2010). The results obtained in this study by varying β are in agreement with this. Slab suction or pressure force induced by overriding plate motion or asthenospheric flow change (Čížková and Bina, 2015; Heuret and Lallemand, 2005) can be cited as candidates for the external force. In addition, trench mobility is necessary to enable these internal and external forces to change the slab morphology (e.g., Christensen, 1996; Nakakuki and Mura, 2013). The viscosity reduction measured by r performs this conversion of the forces to motion: if r is low and lithospheric weakening does not occur, the trench is highly immobile to constrain the subduction velocity, whereas, if r is large, the trench is movable to allow a variable convergence rate (i.e., either advance or retreat) with variable slab morphology.

One of the outliers to the correlation in Fig. 9 is run r2b2: after the collapse of a folded stagnant slab, rapid convergence with the advancing trench appears. This would be attributed to a release of its accumulated potential energy by the sudden slab penetration. Another outlier is the rapid trench retreat associated with slow convergence as is observed at the South Sandwich Islands. The deformable overlying Scotia plate because of the developed back-arc basin seems to contribute to the rapid retreat of the trench. Except for these cases, a dynamic pressure change in the asthenospheric mantle induced by trench movement primarily controls the veloc-

ity of the corresponding induced flows, resulting in the variation of the subduction rate.

The external force is not incorporated into our models, and the deformation of continental margins is also controlled by other factors such as the thickness of the continental lithosphere; therefore, our results cannot be applied to predict unique slab geometries for specific (r, β) pairs. We should, however, note that if r is large, the observed broad variations can be explained by the variation in β. Given the practical meaning of β, i.e., buoyancy owing to the presence of water, a global variation in the water content specific to each subducting slab could account for the variations in Fig. 9. For example, numerous large non-volcanic seamounts occur along the Mariana forearc that originated from serpentinized diapirs produced by slab dehydration (Fryer et al., 1985). Thus, the Mariana slab contains abundant water owing to long-term lithosphere cooling, and the large hydrous buoyancy of the Mariana slab would contribute to its peculiar slab morphology and advancing trench. In addition, subduction of the overlying Philippine sea plate is also essential for both its back-arc spreading and the advancing Mariana trench (Čížková and Bina, 2015). The predominance of retreating slabs and the absence of extremely advancing slabs in actual subduction zones (Fig. 9) imply that buoyant mantle such as serpentinite does not exist widely under the forearc and that less-buoyant hydrous NAMs primarily carry water into deeper mantle if the hydration sufficiently reduces the density of the mantle minerals, as shown by experimental studies (e.g., $\beta = 1.6$; Jacobsen et al., 2008).

4.3. Interpretation of r and β in terms of mineral physics

Traditional deformation experiments have shown that the strain rate $\dot{\varepsilon}$ of hydrous olivine is roughly proportional to the fugacity of water f_{H_2O}, i.e., $r = 1$ (e.g., Hirth and Kohlstedt, 2003), which is consistent with the observation that hydrogen is primarily incorporated as OH^- into the metal sites of olivine to maintain electrical neutrality (Kohlstedt et al., 1996), i.e., $\dot{\varepsilon} \propto [(2H)_M^{\times}]$. On the other hand, recently Fei et al. (2013) revealed the small effect of water on olivine deformation ($r = 1/3$) based on the Si diffusion measurement and proposed that it is controlled by electrically charged vacancies at Si^{4+} and O^{2-} sites. Thus, the site in the olivine structure at which hydrogen is incorporated, which controls how the hydrous crystal deforms, is still being debated. This uncertainty exists because the ion exchange reactions predominant in olivine crystals depend on p-, T-, and f_{H_2O}-conditions, and it is possible that the parameter r is a function of these conditions. Moreover, Fei et al. (2013) attribute the extremely low viscosity of wet olivine observed in previous polycrystalline deformation experiments to excess grain boundary water. If their insistence is valid, the possible range of r in a mantle wedge is wide (i.e., $0.33 \leq r \leq 1.2$) and depends on whether aqueous fluid commonly flows through grain boundaries.

The uncertainty of hydrogen partitioning in NAMs also causes uncertainty about the hydrous buoyancy β as the point defects cause crystal mass loss. Quantification of β may be more complicated because it not only depends on the ionic exchange but also on the ratio of states of water in the mantle. If water is incorporated into dry olivine as fluid inclusions (FI; i.e., exterior to the crystal structure; $r_{diff} = 0$), we rewrite the state equation (16) as

$$\frac{M_{Olv} + M_{H_2O}}{\frac{M_{Olv}}{\rho_{Olv}} + \frac{M_{H_2O}}{\rho_{H_2O}}} = \rho_{Olv}\left(1 - \beta_{FI}\frac{M_{H_2O}}{M_{Olv} + M_{H_2O}}\right), \tag{19}$$

where M is mass and ρ is density. Considering the amount of water to be very small ($M_{H_2O}/M_{Olv} \approx 0$), we obtain

$$\beta_{FI} \approx \frac{\rho_{Olv}}{\rho_{H_2O}} - 1 = 2.30, \tag{20}$$

implying that β_{FI} only depends on the density of the host mineral and fluid inclusions, $\rho_{Olv} = 3{,}300$ [kg/m^3] and $\rho_{H_2O} = 1{,}000$ [kg/m^3], and is much larger than that of synthesized wet olivine (e.g., $\beta = 1.6$; Jacobsen et al., 2008), suggesting that ionic exchange reactions cause β to become smaller. Thus, the form of existence and the dissolution mechanism of H_2O are essential for the ratio of r and β.

4.4. Constraints on water transportation in big mantle wedges

There are some hypotheses on the origin of interplate volcanism such as the Changbaishan ("big mantle wedge"; Zhao et al., 2009). One of these invokes upwellings of buoyant hydrous rocks from the stagnant slab known as wet plumes (e.g., Richard and Iwamori, 2010). Richard and Iwamori (2010) assume that water initially exists directly above the stagnant slab, in contact with the surrounding hotter mantle. However, our simulation shows that, to some extent, the hydrous layer is mechanically coupled with the slab despite heating of the hydrous layer; therefore, a larger viscosity reduction due to hydration r would be necessary for the separation of the plumes. Moreover, large hydrous buoyancy β is required for upwellings of the plumes; however, our simulation shows that large β prevents back-arc spreading, trench retreat, and slab stagnation (Fig. 7). The spontaneous realization of back-arc spreading, stagnant slab, and wet plumes would require some special conditions such as (a) extremely small yield strength along continental margins, which can be split even by a buoyant slab, (b) large negative buoyancy by slab cooling against positive buoyancy of a hydrous layer, and/or (c) extremely localized wet plumes which do not prevent corner flows in a mantle wedge. Testing these conditions would require more detailed 3-D numerical subduction modeling to take into account the toroidal effects during slab stagnation (Schellart and Moresi, 2013). Another explanation is that (d) coincidentally, a stagnant slab and wet plumes are observed simultaneously in spite of a time lag between them. Indeed, our simulation in the case of the large (r, β) pair, such as run r2b2, where wet plumes arise, initially shows slab stagnation at the 660-km phase boundary.

Another hypothesis pertaining to the big mantle wedge invokes aqueous porous flows originating from the dehydration of the stagnant slab (e.g., Ohtani and Zhao, 2009). Porous flows from dehydrated wadsleyite or ringwoodite of the stagnant slab do not affect the solid state flow, rendering it reasonable that a stagnant slab, back-arc spreading (i.e., small β), and water transportation are realized spontaneously. However, dehydration of these minerals may be impossible due to their high water storage capacities (e.g., up to 3.1 wt.% H_2O; Inoue et al., 1995) because the amount of water transported into the mantle transition zone is strictly limited at the "choke point" (Kawamoto et al., 1996). In our runs, the temperature of the hydrous peridotite layers far exceeds this point, and wadsleyite and ringwoodite on the stagnant slab would contain only ~0.2 wt.% H_2O.

5. Conclusions

We have demonstrated that hydrous rocks have multiple effects on subduction dynamics. If hydrous rocks are less viscous (large r), they cause rapid subduction, deformable continental margins, strong trench retreat, and slab stagnation. In contrast, if the hydrous rocks are buoyant (large β), they cause slow subduction, compressional stress on overlying continental plates, trench advance, and slab penetration, all of which are opposite to the effects of r. In other words, the buoyancy of hydrous rocks inhibits subduction by partially canceling out the negative thermal buoyancy of the slab, whereas the low viscosity of hydrous rocks causes the driving force to be transferred to the motion of the mantle by

decoupling the slab from the overlying plate and the surrounding mantle. Our results are consistent with observations of plate motions and slab geometry in natural subduction zones; large r contributes to the diversity of actual subduction zones, whereas β controls the subduction mode including Tonga-type subduction (retreat and stagnation) and Mariana-type subduction (slight advance and penetration) in the case of large r. Thus, the influence of hydrous rocks on subduction dynamics is comparable to that of tectonic forces such as overlying plate motions.

Acknowledgements

Constructive reviews by Dr. Hana Čížková and an anonymous reviewer are greatly appreciated. Numerical simulations were conducted by TSUBAME 2.5 of Tokyo Tech and JAMSTEC SC System. Some figures were produced using Generic Mapping Tools (Wessel and Smith, 1998). This work was supported by JSPS KAKENHI Grant Number 26010035 for A.N. and 26247091 for H.I.

Appendix A. Supplementary material

Supplementary material related to this article can be found online at http://dx.doi.org/10.1016/j.epsl.2016.08.016.

References

Arcay, D., Tric, E., Doin, M.P., 2005. Numerical simulations of subduction zones: effect of slab dehydration on the mantle wedge dynamics. Phys. Earth Planet. Inter. 149, 133–153.

Byerlee, J., 1978. Friction of rocks. Pure Appl. Geophys. 116, 615–626.

Christensen, U.R., 1984. Convection with pressure- and temperature-dependent non-Newtonian rheology. Geophys. J. R. Astron. Soc. 77, 343–384.

Christensen, U.R., 1996. The influence of trench migration on slab penetration into the lower mantle. Earth Planet. Sci. Lett. 140, 27–39.

Christensen, U.R., Yuen, D.A., 1985. Layered convection induced by phase transitions. J. Geophys. Res. 90, 10291–10300.

Čížková, H., Bina, C.R., 2015. Geodynamics of trench advance: insights from a Philippine-Sea-style geometry. Earth Planet. Sci. Lett. 430, 408–415.

Clauser, C., Kiesner, S., 1987. A conservative, unconditionally stable, second-order three-point differencing scheme for the diffusion–convection equation. Geophys. J. Int. 91 (3), 557–568.

Conrad, C.P., Lithgow-Bertelloni, C., 2007. Faster seafloor spreading and lithosphere production during the mid-Cenozoic. Geology 35 (1), 29–32.

Cserepes, L., 1982. Numerical studies of non-Newtonian mantle convection. Phys. Earth Planet. Inter. 30, 49–61.

Dziewonski, A.M., Anderson, D.L., 1981. Preliminary reference Earth model. Phys. Earth Planet. Inter. 25, 297–356.

Fei, H., Wiedenbeck, M., Yamazaki, D., Katsura, T., 2013. Small effect of water on upper-mantle rheology based on silicon self-diffusion coefficients. Nature 498, 213–215.

Fryer, P., Ambos, E.L., Hussong, D.M., 1985. Origin and emplacement of Mariana forearc seamounts. Geology 13, 774–777.

Gerya, T.V., Meilick, F.I., 2011. Geodynamic regimes of subduction under an active margin: effects of rheological weakening by fluids and melts. J. Metamorph. Geol. 29, 7–31.

Heuret, A., Lallemand, S., 2005. Plate motions, slab dynamics and back-arc deformation. Phys. Earth Planet. Inter. 149, 31–51.

Hirth, G., Kohlstedt, D., 2003. Rheology of the upper mantle and the mantle wedge: a view from the experimentalists. In: Eiler, J. (Ed.), Inside the Subduction Factory, pp. 83–105.

Horiuchi, S., Iwamori, H., 2016. A consistent model for fluid distribution, viscosity distribution, and flow-thermal structure in subduction zone. J. Geophys. Res., Solid Earth 121, 3238–3260.

Inoue, T., Weidner, D.J., Northrup, P.A., Parise, J.B., 1998. Elastic properties of hydrous ringwoodite (γ-phase) in Mg_2SiO_4. Earth Planet. Sci. Lett. 160, 107–113.

Inoue, T., Yurimoto, H., Kudoh, Y., 1995. Hydrous modified spinel, $Mg_{1.75}SiH_{0.5}O_4$: a new water reservoir in the mantle transition region. Geophys. Res. Lett. 22, 117–120.

Iwamori, H., 1998. Transportation of H_2O and melting in subduction zones. Earth Planet. Sci. Lett. 160, 65–80.

Iwamori, H., 2007. Transportation of H_2O beneath the Japan arcs and its implications for global water circulation. Chem. Geol. 239, 182–198.

Jacobsen, S.D., Jiang, F., Mao, Z., Duffy, T.S., Smyth, J.R., Holl, C.M., Frost, D.J., 2008. Effects of hydration on the elastic properties of olivine. Geophys. Res. Lett. 35, L14303.

Karato, S., 2011. Water distribution across the mantle transition zone and its implications for global material circulation. Earth Planet. Sci. Lett. 301, 413–423.

Karato, S., Jung, H., 1998. Water, partial melting and the origin of seismic low velocity and high attenuation zone in the upper mantle. Earth Planet. Sci. Lett. 157, 193–207.

Karato, S., Wu, P., 1993. Rheology of the upper mantle: a synthesis. Science 260, 771–778.

Kawamoto, T., Herving, R.L., Holloway, J.R., 1996. Experimental evidence for a hydrous transition zone in the early Earth's mantle. Earth Planet. Sci. Lett. 142, 587–592.

Kohlstedt, D.L., Evans, B., Mackwell, S.J., 1995. Strength of the lithosphere: constraints provided by the experimental deformation of the rocks. J. Geophys. Res. 100, 17587–17602.

Kohlstedt, D.L., Keppler, H., Rubie, D.C., 1996. Solubility of water in the α, β and γ phases of $(Mg,Fe)_2SiO_4$. Contrib. Mineral. Petrol. 123, 345–357.

Korenaga, J., Karato, S., 2008. A new analysis of experimental data on olivine rheology. J. Geophys. Res. 113, B02403.

Lallemand, S., Heuret, A., Faccenna, C., Funiciello, F., 2008. Subduction dynamics as revealed by trench migration. Tectonics 27, TC3014.

Mackwell, S.J., Kohlstedt, D.L., 1990. Diffusion of hydrogen in olivine: implications for water in the mantle. J. Geophys. Res. 95, 5079–5088.

Mao, Z., Jacobsen, S.D., Jiang, F., Smyth, J.R., Holl, C.M., Duffy, T.S., 2008. Elasticity of hydrous wadsleyite to 12 GPa: implications for Earth's transition zone. Geophys. Res. Lett. 35, L21305. http://dx.doi.org/10.1029/2008GL035618.

Murakami, M., Hirose, K., Yurimoto, H., Nakashima, S., Takafuji, N., 2002. Water in the Earth's lower mantle. Science 295, 1885–1887.

Nakakuki, T., Mura, E., 2013. Dynamics of slab rollback and induced back-arc basin formation. Earth Planet. Sci. Lett. 361, 287–297.

Ohtani, E., Zhao, D., 2009. The role of water in the deep upper mantle and transition zone: dehydration of stagnant slabs and its effects on the big mantle wedge. Russ. Geol. Geophys. 50, 1073–1078.

Okuno, J., Nakada, M., 2001. Effects of water load on geophysical signals due to glacial rebound and implication for mantle viscosity. Earth Planets Space 53, 1121–1135.

Patankar, S.V., 1981. A calculation procedure for two-dimensional elliptic situations. Numer. Heat Transf. 4, 409–425.

Richard, G.C., Iwamori, H., 2010. Stagnant slab, wet plumes and Cenozoic volcanism in East Asia. Phys. Earth Planet. Inter. 183, 280–287.

Royden, L.H., Husson, L., 2006. Trench motion, slab geometry and viscous stresses in subduction systems. Geophys. J. Int. 167, 881–905.

Rüpke, L.H., Morgana, J.P., Hortb, M., Connolly, J.A.D., 2004. Serpentine and the subduction zone water cycle. Earth Planet. Sci. Lett. 223, 17–34.

Schellart, W.P., 2008. Kinematics and flow patterns in deep mantle and upper mantle subduction models: influence of the mantle depth and slab to mantle viscosity ratio. Geochem. Geophys. Geosyst. 9, Q03014.

Schellart, W.P., 2011. A subduction zone reference frame based on slab geometry and subduction partitioning of plate motion and trench migration. Geophys. Res. Lett. 38, L16317.

Schellart, W.P., Moresi, L., 2013. A new driving mechanism for backarc extension and backarc shortening through slab sinking induced toroidal and poloidal mantle flow: results from dynamic subduction models with an overriding plate. J. Geophys. Res., Solid Earth 118, 3221–3248.

Stegman, D.R., Farrington, R., Capitanio, F.A., Schellart, W.P., 2010. A regime diagram for subduction styles from 3-D numerical models of free subduction. Tectonophysics 483, 29–45.

Steinberger, B., Sutherland, R., O'Connell, R.J., 2004. Prediction of Emperor–Hawaii seamount locations from a revised model of global plate motion and mantle flow. Nature 430, 167–173.

Sun, W., Yoshino, T., Sakamoto, N., Yurimoto, H., 2015. Hydrogen self-diffusivity in single crystal ringwoodite: implications for water content and distribution in the mantle transition zone. Geophys. Res. Lett. 42, 6582–6589.

Tackley, P.J., 2000. Self-consistent generation of tectonic plate in time-dependent, three-dimensional mantle convection simulations 1. Pseudoplastic yielding. Geochem. Geophys. Geosyst. 1.

Tagawa, M., Nakakuki, T., Kameyama, M., Tajima, F., 2007. The role of history-dependent rheology in plate boundary lubrication for generating one-sided subduction. Pure Appl. Geophys. 164, 1–29.

Turcotte, D.L., Schubert, G., 2001. Geodynamics. Cambridge University Press.

Van der Lee, S., Regenauer-Lieb, K., Yuen, D.A., 2008. The role of water in connecting past and future episodes of subduction. Earth Planet. Sci. Lett. 273, 15–27.

Wannamaker, P.E., Caldwell, T.G., Jiracek, G.R., Maris, V., Hill, G.J., Ogawa, Y., Bibby, H.M., Bennie, S.L., Heise, W., 2009. Fluid and deformation regime of an advancing subduction system at Marlborough, New Zealand. Nature 460, 733–736.

Wessel, P., Smith, W.H.F., 1998. New, improved version of the Generic Mapping Tools released. EOS Trans. Am. Geophys. Union 79, 575–579.

Yamasaki, T., Seno, T., 2003. Double seismic zone and dehydration embrittlement of the subducting slab. J. Geophys. Res. 108 (B4), 2212. http://dx.doi.org/10.1029/2002JB001918.

Zhao, D., Tian, Y., Lei, J., Liu, L., Zheng, S., 2009. Seismic image and origin of the Changbai intraplate volcano in East Asia: role of big mantle wedge above the stagnant Pacific slab. Phys. Earth Planet. Inter. 173, 197–206.